Int J CARS (2011) 6:119–126
DOI 10.1007/s11548-010-0487-7

ORIGINAL ARTICLE

Toward a clinical lumbar CAD: herniation diagnosis

Raja' S. Alomari · Jason J. Corso · Vipin Chaudhary · Gurmeet Dhillon

Received: 12 January 2010 / Accepted: 4 May 2010 / Published online: 11 June 2010

Abstract
Purpose A CAD system for lumbar disc degeneration and herniation based on clinical MR images can aid diagnostic decision-making provided the method is robust, efficient, and accurate.
Material and methods A Bayesian-based classifier with a Gibbs distribution was designed and implemented for diagnosing lumbar disc herniation. Each disc is segmented with a gradient vector flow active contour model (GVF-snake) to extract shape features that feed a classifier. The GVF-snake is automatically initialized with an inner boundary of the disc initiated by a point inside the disc. This point is automatically generated by our previous work on lumbar disc labeling. The classifier operates on clinical T2-SPIR weighted sagittal MRI of the lumbar area. The classifier is applied slice-by-slice to tag herniated discs if they are classified as herniated in any of the 2D slices. This technique detects all visible herniated discs regardless of their location (lateral or central). The gold standard for the ground truth was obtained from collaborating radiologists by analyzing the clinical diagnosis report for each case.
Results An average 92.5% herniation diagnosis accuracy was observed in a cross-validation experiment with 65 clinical cases. The random leave-out experiment runs ten rounds; in each round, 35 cases were used for testing and the remaining 30 cases were used for training.
Conclusion An automatic robust disk herniation diagnostic method for clinical lumbar MRI was developed and tested. The method is intended for clinical practice to support reliable decision-making.

Keywords Lumbar spine · Clinical MRI · CAD · GVF-snake · Active contour · Gibbs distribution · Bayes model

R. S. Alomari (✉) · J. J. Corso · V. Chaudhary
Department of Computer Science and Engineering,
SUNY at Buffalo, Buffalo, NY 14260, USA
e-mail: ralomari@buffalo.edu

G. Dhillon
ProScan Imaging of Buffalo, Williamsville, NY 14221, USA

Introduction

Lumbar disc herniation is the major intervertebral disc disease (IDD) that causes mobility limitation and intolerable pain levels. IDD is the reason for over 90% of surgical spine procedures [1]. Furthermore, over 12 million Americans have some sort of IDD according to the National Institute of Neurological Disorders and Stroke (NINDS) [2]. They spend at least $50 billion each year on medical diagnosis and rehabilitations related to the lower back pain [2].

Computer-aided diagnosis (CAD) systems have been attracting many researchers in various human organs such as using MRI for detection of breast cancer [3] and prostate cancer [4]. Surprisingly, there has been no clinically useful CAD system for lumbar area diagnosis despite that lumbar abnormalities are the major activity limitation reason for people under 45 besides the intolerable amount of pain. To that end, work on designing a full CAD system for the lumbar area that will utilize the radiologists time and diagnosis efficiency.

In this paper, we continue our efforts [5–9] in designing a clinical CAD system for lumbar disc degeneration. We present our approach for herniation diagnosis based on segmentation of the discs from T2-SPIR sagittal MRI images and extraction of suitable shape features that identify the herniated discs. We start by our automatic localization and labeling step [5] that results in a point inside the disc. Then,

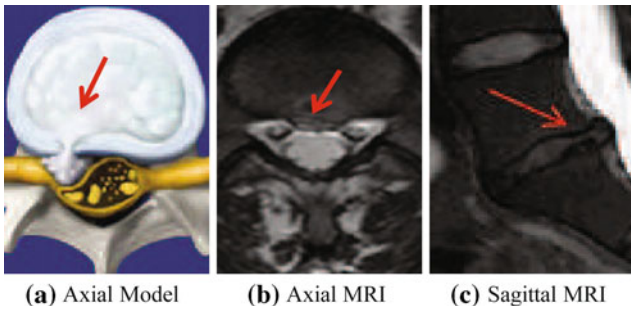

Fig. 1 **a** A *right*-sided disc herniation illustrative model [11]. **b** Axial view (*bottom-up*) MRI of a *right*-sided disc herniation from our data. **c** Corresponding sagittal view of the herniated disc from our dataset

we utilize the low signal of the disc boundary that appears in T2-SPIR sagittal MRI to initiate an active contour model (GVF-Snake) [10]. After delineation of the disc boundary, we extract shape features to train a Gibbs distribution Bayes model similar to our previous work [8]. Figure 1 shows a herniated disc from both axial and sagittal views for the same disc.

We, however, point out that the nomenclature has been developing and changing over the last decade since Fardon and Milette [12] initiated their lumbar disc pathology nomenclature. We use the term "disc herniation" to refer to "Localized displacement of disc material beyond the normal margins of the intervertebral disc space" [12]. Our collaborative clinical radiologist uses the term *disc herniation* to refer to this same problem. We further define it as the leak of the inner gel-like disc material, *nucleus pulposus*, (as shown in Fig. 1) through any tear in the outer fibrous disc ring, *annulus fibrosus*, which extends beyond the normal margins of the disc space. Disc herniation causes pressure on the nerve root resulting in the pain and numbness to the patient where the pain, most of the time, irritates to the knees causing major disruption of the patient's life. The development of the term of disc herniation includes the terms: disc bulging, protrusion, and extrusion [13]. We also point out that the nomenclature of Fardon and Milette [12] has been endorsed by the major American and European radiologists associations including ASSR, ASNR, AANS, CNS, ESNR, and many others.

The remainder of this paper presents a background and related work in Sect. 2. We detail our method and our Gibbs-based classifier in Sect. 3. Then, we describe the available data in Sect. 4. In Sect. 5, we present our experimental settings and results and we conclude in Sect. 6.

Background and related work

Discs have two main components: an outer fibrous ring, *annulus fibrosus*, and an inner gel-like material, *nucleus pulposus*. Disc herniation starts with a tear in the annulus fibrosus causing part of the nucleus pulposus to leak out pressing on a nerve root as shown in the illustrative model in Fig. 1a. Disc herniation is usually caused by disc degeneration or other traumatic reasons. As time passes, the disc herniation worsens and the leak increases if proper actions are not taken causing disruption in the patient's mobility [14].

Many researchers have proposed methods for the diagnosis of certain vertebral column abnormalities. Bounds et al. [15] utilized a neural network for diagnosis of back pain and sciatica. Sciatica might be caused by lumbar disc herniation as well as many other reasons. They have three groups of doctors to perform diagnosis as their validation mechanism. They achieved better accuracy than the doctors in the diagnosis. However, the lack of data prohibited them from full validation of their system. Similarly, Vaughn [16] conducted a research study on using neural network for assisting orthopedic surgeons in the diagnosis of lower back pain. They classified LBP into three broad clinical categories. They used 25 features to train the neural network (NN) including symptoms clinical assessment results. The NN achieved 99% of training accuracy and 78.5% of testing accuracy. This clearly shows training data overfitting.

Tsai et al. [17] used geometrical features (shape, size, and location) to diagnose herniation from 3D MRI and CT axial (transverse sections) volumes of the discs. In contrast, we do not presume the availability of the full volume axial view as it is not a clinical standard. They patented their work as a visualization tool for educational purposes.

Recently, Michopoulou et al. [18] applied three variations of fuzzy c-means (FCM) to perform atlas-based disc segmentation. Then, they used this segmentation for classification of the disc as either a normal or degenerative disc. They did not mention any details of the classification scheme other than it is a Bayesian classifier. However, they achieved 86–88% classification accuracy on 34 cases (five discs each) based on their semi-automatic segmentation of the disc. We, however, have a fully automatic segmentation of the disc, and we extract shape features from modeling the disc shape and delineating the herniated segment of the disc.

In our most recent work, Alomari et al. [9], we presented herniation detection using two co-registered sagittal views of T1 and T2-weighted MRI. We utilized an active shape model (ASM) to roughly segment the disc and then jointly model certain shape and intensity features. Despite the robust and good results, training the ASM was time-consuming, and we wanted to reduce the manual burden of training and selection of the suitable shape features. In this paper, we utilize another feature of the T2-SPIR MRI images where there is a low-signal boundary of the discs that gives a good initial contour of the disc. The GVF-snake delineates this contour and help remove all excessive and unnecessary edges. Then, we model the two major axes of the semi-elliptical resulting shape to train our Bayes classifier.

Method

Our herniation diagnosis approach has four steps as follows:

1. Disc localization: This step produces a point inside the each disc along with the anatomical names discussed in Sect. 3.1.
2. Disc edge map: We produce an initial boundary of the disc (edge map) by thresholding the low signal appears in the T2-SPIR MRI as discussed in Sect. 3.2.
3. Disc segmentation: We use GVF-snake, initiated by the initial boundary, to finely segment the disc as discussed in Sect. 3.3.
4. Herniation classification: Using shape features, only, extracted from the GVF-snake, we design a Gibbs-based classifier to classify each disc with either normal or herniated as discussed in Sect. 3.4.

Disc localization

We use our automatic labeling approach [19,5] that provides a point inside each disc using our two-level probabilistic model. Our model labels the set of discs with high-level labels $\mathtt{D} = \{d_1, d_2, \ldots, d_6\}$ where each $d_i = (x_i, y_i)^{\mathsf{T}}$ is the coordinates of the disc point (some point in the disc). Then, we solve the optimization problem:

$$\begin{aligned} \mathtt{D}^* &= \arg\max_{\mathtt{D}} \sum_{\mathtt{L}} P(\mathtt{L}, \mathtt{D}|\mathtt{I}) \\ &= \arg\max_{\mathtt{D}} \sum_{\mathtt{L}} \frac{P(\mathtt{I}|\mathtt{D}, \mathtt{L}) P(\mathtt{D}, \mathtt{L})}{P(\mathtt{I})} \\ &= \arg\max_{\mathtt{D}} \sum_{\mathtt{L}} P(\mathtt{I}|\mathtt{L}) P(\mathtt{L}|\mathtt{D}) P(\mathtt{D}) \end{aligned} \quad (1)$$

where $\mathtt{L} = \{l_i, \ \forall i \in \mathrm{L}\}$ is a set of auxiliary variables, called disc-label variables that are introduced to infer $\mathtt{D}$ from the sagittal image. Each disc-label variable can take a value of $\{-1, +1\}$ for non-disc or disc, respectively. The disc-labels make it plausible to separate the disc variables from the image intensities, i.e., the disc-label $\mathtt{L}$ variables capture the local pixel-level intensity models, while the disc variables $\mathtt{D}$ capture the high-level geometric and contextual models of the full set of discs. The optimization is solved with a generalized expectation minimization (gEM) algorithm [5]. Figure 2 shows a lumbar sagittal view with labeled discs.

Then, we obtain a fixed window of 60×120 pixels around each point. This sub-image size is enough to provide the whole disc region for each of the discs connected to the five lumbar vertebrae as shown in Figs. 2 and 3.

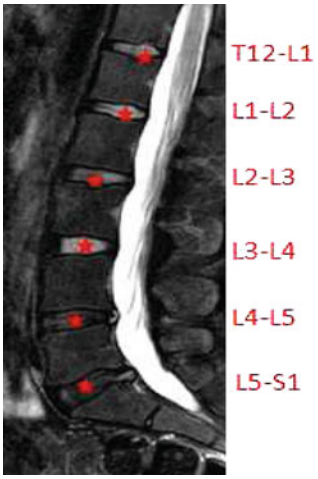

Fig. 2 Labeling lumbar discs in a sagittal T2-weighted MRI

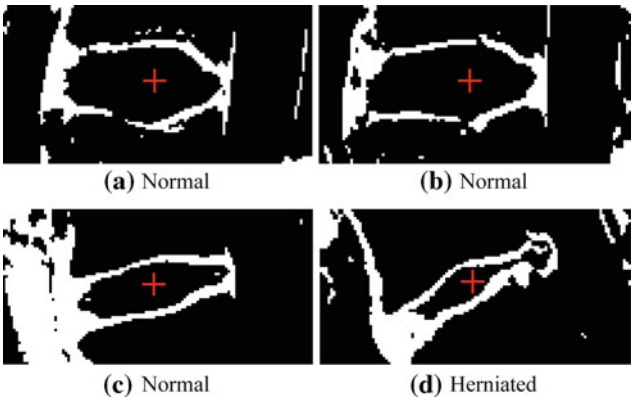

Fig. 3 Edge map generation utilizing the low-signal intensity of the disc boundary in T2-SPIR MRI. Boundary is enhanced (by bolding) for visual clarity

Disc edge map

Figure 2 shows the low-intensity signal surrounding each disc. This low signal is distinguished in the T2-SPIR MR images and more apparent that all other MRI protocols. It provides a robust edge map for the disc as shown in Fig. 3. This simple thresholding step produces undesirable edges as well. However, all these edges are outside the disc because of the relatively higher intensity signal of the disc body even with degenerated discs.

Thus, we use both the point inside the disc (step 1) and this initial contour (step 2) to initiate the GVF-snake from within the disc. This guarantees that the final disc segmentation lies within the disc and thus a successful segmentation.

Disc segmentation

We use an active contour to delineate the disc boundaries. We select the GVF-snake proposed by Xu and Prince [10]

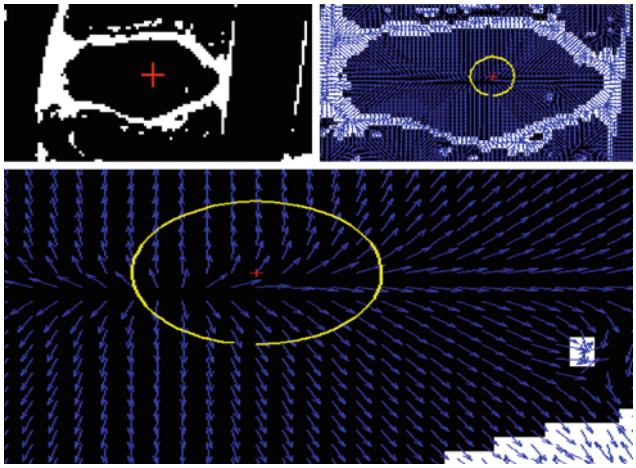

Fig. 4 (*Top-left*) Shows the edge map. (*Top-right*) The corresponding normalized GVF field showing the localization point. (*Bottom*) A zoomed version of the GVF field to clearly show the vectors

because it has been proved to move toward desired image properties such as edges including concavities. GVF-snake is the parametric curve that solves:

$$\mathbf{x}_t(s,t) = \alpha \mathbf{x}''(s,t) - \beta \mathbf{x}''''(s,t) + \mathbf{v} \tag{2}$$

where α and β are weighting parameters that control the contour's tension and rigidity, respectively. x'' and x'''' are the second and fourth derivatives, respectively, of x. $\mathbf{v}(x, y)$ is the gradient vector flow (GVF), $s \in [0, 1]$, and t is time component to make a dynamic snake curve from $x(s)$ yielding $x(s, t)$.

GVF-snake requires an edge map that is a binary image highlighting the desired features (edges) of the image. Most researchers use Canny edge detector or Sobel operator on the original image such as [20] for liver segmentation. We present the GVF-snake with our edge map produced in (step 2).

We apply the GVF-snake by initializing its contour to a small circle surrounding the disc point produced from step 1. The edge map then drives this small circle to delineate the initial edge map resulting in an inner segmentation of the disc. This also excludes all undesirable edges appear in the edge maps. Figure 4 shows an example of a disc with its GVF field and a zoomed version to show the directions of the arrows.

Herniation classification

We design a binary Bayesian classifier:

$$n^* = \arg\max_n P(n|\mathtt{S}) \tag{3}$$

where n is a binary random variable stating whether it is a herniated or a normal disc, $\mathtt{S}$ incorporates shape features extracted from GVF-snake final contour. We utilize a Gibbs distribution with two shape potentials:

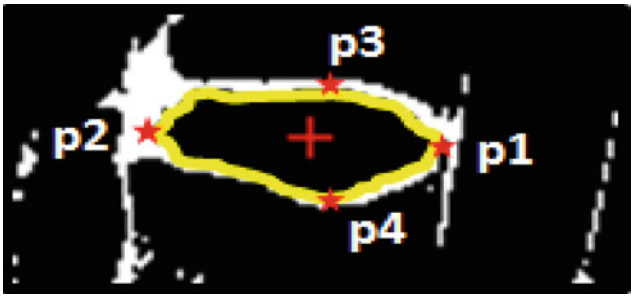

Fig. 5 *Yellow* contour is the final GVF-snake contour. Points p1–p4 are shown. Contours are *bolded* for clarity

$$P(n|\mathtt{S}) = \frac{1}{Z[n]} \exp^{-[\alpha_1 U_{\mathtt{S}_1} + \alpha_2 U_{\mathtt{S}_2}]} \tag{4}$$

where $\mathtt{S}$ represents the shape features extracted from the GVF-snake, $Z[n]$ is the normalization factor of the Gibbs distribution, α_1 and α_2 are tuning parameters. We define two shape potentials: (1) $U_{\mathtt{S}_1}$ models the major axis of the GVF-snake final contour. (2) $U_{\mathtt{S}_2}$ models the minor axis of the GVF-snake final contour.

We extract the first shape potential $U_{\mathtt{S}_1}$ from measuring the GVF-snake major axis. This distance represents the distance between the farthest two points in each direction on the x-axis of the image. Because we always start our initial contour from within the disc, the extreme x-axis points represent the major axis of the disc. Thus, we define the major distance e_1:

$$e_1 = |p_1 - p_2|_2 \tag{5}$$

where the points p_1 and p_2 represent the extreme x-axis points as shown in Fig. 5.

Similarly, we extract the second shape potential $U_{\mathtt{S}_2}$ from the minor axis by measuring distance between the extreme y-axis points. Thus, we define the minor distance e_2:

$$e_2 = |p_3 - p_4|_2 \tag{6}$$

where the points p_3 and p_4 represent the extreme y-axis points as shown in Fig. 5.

We model both potentials $U_{\mathtt{S}_1}$ and $U_{\mathtt{S}_2}$ with Gibbs distributions similar to our previous work [8]:

$$U_{\mathtt{S}_1} = \frac{(e_1 - \mu_{e_1})^2}{2\sigma_{e_1}^2} \tag{7}$$

where e_1 is the major axis from the GVF-contour, $\mu_{e_1}\sigma_{e_1}^2$ are the expected and the variance of the major axis distance, respectively. We estimate both μ_{e_1} and $\sigma_{e_1}^2$ from the training data.

$$U_{\mathtt{S}_2} = \frac{(e_2 - \mu_{e_2})^2}{2\sigma_{e_2}^2} \tag{8}$$

where e_2 is the disc minor axis length, μ_{e_2} is the expected minor axis length of the disc, $\sigma^2_{e_2}$ is the variance of the minor axis length of the disc. We learn both μ_{e_2} and $\sigma^2_{e_2}$ from the training data.

Available data

We validate our work on a clinical MRI dataset captured by a Philips 3-Tesla scanner. The subjects range in their age between 17 and 81 years old with various abnormality conditions including at least one herniated disc in each subject. The data for each subject is the standard clinical settings that include T1, T2, and Myelo.

In the clinical settings, the MRI technician usually acquires two sagittal views (T1- and T2-weighted). Then, she acquires six axial T1-weighted slices that span each disc (slice inter-space is about 0.5 mm). She makes sure that the patient does not move during the whole acquisition process, which takes about 24 min, to have all imaging protocols manually registered. She also acquires Myelo MRI which is usually used for spinal related diseases such as spinal stenosis.

It is a known practice to reduce the effect of the magnetic field inhomogeneities in MRI by normalizing the intensity to a standard reference. This reference can be either the cerospinal spinal fluid (CSF) [21] or the spinal signal [22]. We pre-process all our data by normalizing the intensity using the spine signal to avoid related issues of magnetic field inhomogeneities.

Similar to all medical image analysis, we face the challenge of the ground truth determination due to inter-observer variability. However, it has been studied that MRI has high inter-observer reliability compared to plain X-ray radiographs in diagnosis of lumbar area abnormalities, which indicates higher agreement between radiologists when diagnosing MRI than X-rays radiographs. For example, Mulconrey et al. [23] showed that abnormality detection for degenerative disc and Spondylolisthesis with MRI has $\kappa = 0.773$ and $\kappa = 0.728$, respectively, which is considered high in showing inter-observer reliability where this reliability is considered perfect when $0.8 \leq \kappa \leq 1$.

Our collaborating clinical research group provides us with the clinical diagnosis reports that specify the abnormalities at each disc level. A sample report portion is shown in Fig. 6. We use these reports as our gold standard for validating our classifier.

Table 1 shows the acquisition parameters for our dataset.

Experimental results

We validate our method on 65 clinical MRI cases. Each case has at least one herniated disc and the rest are normal. In each case, there are six discs connected to the five lumbar vertebrae as shown in Fig. 2.

Type of exam:	MR-Lumbar spine w/o contrast.
Date of birth:	DELETED FOR ANONYMITY.
History:	Backpain.
Findings:	At the L5-S1 level, there is a 6mm right paracentral disc herniation indenting the anterior aspect of the thecal sac and impinging on the right S1 nerve root in the recess. The neural foramina are patent. The L4-5, L3-4, L2-3, L1-2, and T12-L1 levels show no evidence of disc herniation or spinal stenosis. The neural foramina are patent. The conus and cauda equina are normal. The paravertebral soft tissues are normal. No fracture or dislocation is identified.

Fig. 6 Sample portion of the clinical diagnosis report showing the diagnosis at each disc level of lumbar area. We use these reports as our gold standard

Table 1 MRI protocols parameters for our dataset

Parameter	T2-SPIR	T1	Mayelo
Repetition time (TR) (ms)	3,157	618	8,000
Echo time (TE) (ms)	100	7.2	1,000
Flip angle (degree)	90	90	90

We perform a cross-validation experiment using the 65 cases to validate our proposed method. In each round, we separate 35 cases for testing and train on the remaining 30 cases. We perform 10 rounds and each time, we randomly select the cases. We define:

$$\text{Accuracy}_\text{i} = (1 - \frac{1}{K}\sum_{j=1}^{K} |g_{ij} - n_{ij}|) * 100\% \quad (9)$$

where Accuracy_i represents the classification accuracy (herniated disc detection) at the lumbar disc level i where $1 \leq i \leq 6$, K is the testing set size in each round (30 cases), g_{ij} is the ground truth binary assignment for disc i in case j, and n_{ij} is the resulting binary assignment for disc i from the inference on our model. The binary variables g_i and n_i are assigned the binary values such that they are 0 if i is a normal disc and 1 if it is a herniated disc.

Table 2 Results of the cross-validation experiment with an average detection accuracy of 92.5%

Set	L5-S1	L4-5	L3-4	L2-3	L1-2	T12-L1	Avg (%)
1	31	30	32	33	34	32	91
2	33	33	30	32	32	33	92
3	32	31	32	30	33	34	91
4	33	34	32	32	33	34	94
5	32	34	32	33	33	33	94
6	31	32	32	31	32	33	91
7	33	32	34	34	33	33	95
8	31	31	31	33	30	34	91
9	33	33	30	34	34	32	93
10	31	34	33	33	32	33	93
%	91.4	92.6	90.9	92.9	93.1	94.3	–
Average accuracy							**92.5**

Table 2 shows the classification results from the cross-validation experiment. We achieve an average classification accuracy of 92.5%. The table also shows the accuracy at each lumbar level (column) in each cross-validation round (row).

We further compute the overall specificity and sensitivity where:

$$\text{Specificity} = \frac{TN}{TN + FP} \tag{10}$$

$$\text{Sensitivity} = \frac{TP}{TP + FN} \tag{11}$$

where FP is the number of false positives (normal discs diagnosed as herniated), TP is the number of true positives (correctly diagnosed herniated discs), FN is the number of false negatives (misclassified herniated discs), and TN is the number of true negatives (correctly classified normal discs).

On the other hand, we compare our shape-based classifier to a Bayesian classifier [18] that only models the disc intensity. Our shape-based classifier substantially outperforms the intensity-based classifier. To show a fair comparison, we run the same cross-validation experiment shown in Table 2 on the intensity-based classifier. The average classification accuracy did not exceed 81%. We justify this by the observation

Table 3 Calculation of specificity (96.6%) of and sensitivity (86.4%)

Result	Gold standard	
	Herniated	Normal
Herniated	481 (TP)	76 (FP)
Normal	53 (FN)	1,490 (TN)

that despite herniated discs lose intensity levels, this loss is insufficient to feed in a classifier and thus detect herniation based on intensity. Thus, shape is more important in the case of herniation and this is what the empirical results are leading us to conclude. To clarify this situation, Fig. 7 (Right) shows a sample herniated disc, with high intensity level, that was misclassified by the intensity-based classifier but correctly classified with our shape-based classifier. Figure 7 (Left) shows low-intensity herniated disc that is correctly classified with both classifiers (Table 3).

Our classification model directly employs shape (steps 3 and 4) information and indirectly employs intensity (step 2) information. The thresholding step (#2) has limitation due to MRI signal noise and inhomogeneity. Thus, the edge map produced by this step might limit the ability of the GVF-snake to converge to an exact disc boundary. However, our classification model does not depend on an accurate segmentation of the disc as opposed to Michopoulou et al [18]. Instead, we only rely on four points from the converged GVF-snake segmentation: the top, bottom, most-right, and most left to feed in our classifier model. Our empirical study shows high robustness for our herniation detection that ranges between 91 and 95% as shown in Table 2.

Figure 8 shows two sample cases with successful diagnosis at all lumbar disc levels. In the first case, the lower two discs (L4-5 and L5-S1) are herniated, while the rest are clinically normal. The thresholding step works perfectly for both cases as well as the extraction of both shape potentials. The second case has one herniated disc at L4-5 level, while the rest are clinically normal. Despite that the L4-5 disc level is not an extreme herniation (diagnosed with 2-mm herniation), our automated method successfully classified the disc as herniated.

Fig. 7 (*Left*) Low-intensity herniated disc. (*Right*) High intensity herniated disc

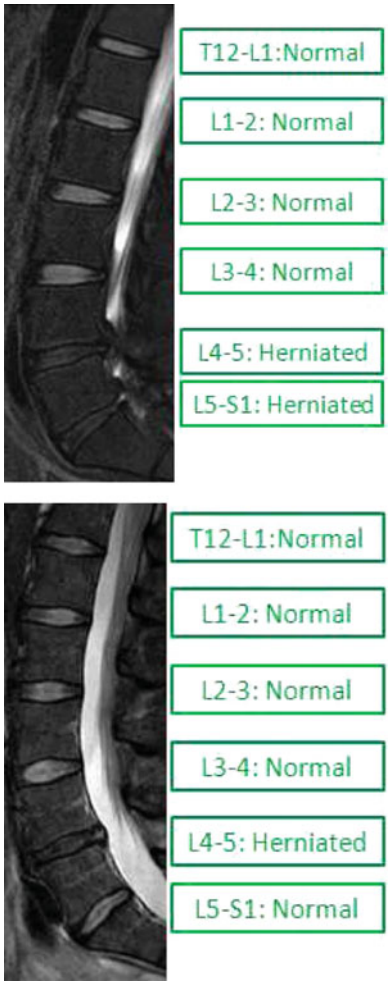

Fig. 8 Two successfully diagnosed cases

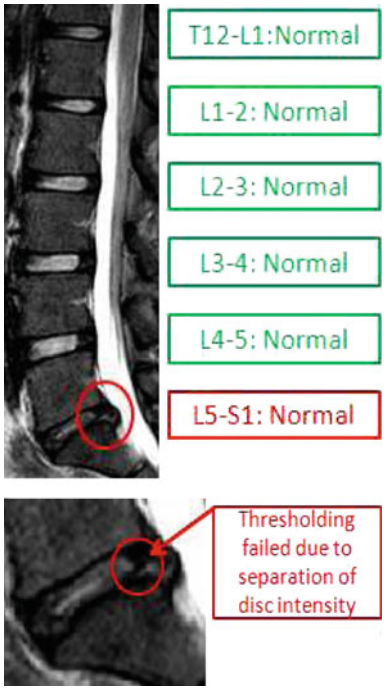

Fig. 9 Unsuccessful diagnosis at L5-S1 disc level. The zoomed version of the disc shows a line of low intensity marked by the *red circle*. This lined cause error in the second step and thus misled the shape potential

Figure 9 shows a case where the lower lumbar disc has a special case that caused failure in automated herniation detection. As we show in the zoomed version of the L5-S1 disc, the disc nucleous pulposus intensity is separated by a line of low intensity. The disc seems as two separate parts. This very rare case misled step 2 of our method where we perform thresholding to produce the edge map for the GVF-snake. Because of the failure of the thresholding step, the shape potentials were misled and considered the larger disc segment as a normal disc. However, this is a very rare clinical case and usually the patient suffers huge pain that needs special attention from the radiologist.

Conclusion

We proposed a method for herniation diagnosis from clinical lumbar MRI. Our Bayes classifier is based on shape features extracted from delineated GVF-snakes. However, it indirectly employs intensity information by utilizing a thresholding preprocessing step to prepare the edge map for the GVF-snake. We validate our method on the T2-SPIR MRI protocol as the disc intensity is best distinguished from other structures.

Initially, we localize the discs from sagittal slices using our previous method where we automatically localize a point inside each disc. Then, we apply a thresholding step to extract the edge map for the GVF-snake. We then automatically initialize the GVF-snake with a small circle around the localized point inside the disc. After the convergence of the GVF-snake, we extract two shape potentials that we use to diagnose each disc upon our trained Bayes classifier model.

We validated our method on 65 clinical MRI cases and achieved an average accuracy of 92.5% on a cross-validation experiment across all lumbar discs. Our diagnosis accuracy is higher at the three upper discs (T12-L1, L1-2, and L2-3) with an average of 94.3, 93.1, and 92.9%, respectively. We obtained an average diagnosis accuracy at the lower levels L3-4, L4-5, and L5-S1 of 90.9, 92.6, and 91.4%, respectively. On the same experiment, we achieved 96.6% specificity and 86.4% sensitivity.

Acknowledgment This work was supported, in part, by Dr. Chaudhary grant from the New York State Foundation for Science, Technology and Innovation (NYSTAR) and by Dr. Corso NSF CAREER grant IIS 0845282.

References

1. An H, Anderson P, Haughton V, Iatridis J, Kang J, Lotz J, Natarajan R, Oegema T, Roughley P, Setton L, Urban J, Videman T, Andersson G, Weinstein J (2004) Introduction. disc degeneration: summary. Spine 29:2677–2678
2. NINDS (2008) National institute of neurological disorders and stroke (ninds): low back pain fact sheet, NIND brochure
3. iCAD (2009) Spectra look digital from icad, Computer aided diagnosis, http://www.icadmed.com/breastmri.htm
4. iCAD (2009) Vivid look from icad, Computer aided diagnosis, http://www.icadmed.com/prostatemri.htm
5. Corso JJ, Alomari RS, Chaudhary V (2008) Lumbar disc localization and labeling with a probabilistic model on both pixel and object features. In Proceedings of MICCAI. vol 5241 of LNCS Part 1, pp 202–210, Springer
6. Alomari Raja' S, Corso Jason J, Chaudhary V (2009) Abnormality detection in lumbar discs from clinical mr images with a probabilistic model, In Proceedings of CARS
7. Alomari Raja' S, Corso Jason J, Chaudhary V, Dhillon G (2009) Desiccation diagnosis in lumbar discs from clinical mri with a probabilistic model, In Proceedings of ISBI'09, pp 546–549
8. Alomari Raja' S, Corso Jason J, Chaudhary V, Dhillon G (2009) Computer-aided diagnosis of lumbar disc pathology from clinical lower spine mri. Int J Comput Assist Radiol Surg (in press)
9. Alomari Raja' S, Corso Jason J, Chaudhary V, Dhillon G (2010) Automatic diagnosis of disc herniation with shape and appearance features from mri, In Proceedings of SPIE'10, to appear
10. Xu Chenyang, Prince Jerry L (2000) Handbook of medical imaging. Academic Press, Baltimore 159–169
11. Swarm (2007) Interactive incorporation (viewmedica)—patient educatuion system
12. Fardon David F, Milette Pierre C (2001) Nomenclature and classification of lumbar disc pathology. SPINE 26(5):E93–E113
13. Fardon David F, Milette Pierre C (2001) Nomenclature and classification of lumbar disc pathology, AJNR, http://www.asnr.org/spine_nomenclature/glossary.shtml
14. Snell Richard S (2007) Clinical Anatomy by Regions, Lipp. Will. and Wilkins, 8th edn
15. Bounds DG, Lloyd PJ et al (1988) A multilayer perceptron network for the diagnosis of low back pain, In Proceedings of Conference on Neural Networks, San Diego, CA, July vol 2, pp 481–489.
16. Vaughn M (2000) Using an artificial neural network to assist orthopaedic surgeons in the diagnosis of low back pain, in http://www.marilyn-vaughn.co.uk/lbpainresearchstudy.htm, Dept. of Inf., Cranfield University (RMCS), June 2000
17. Tsai M et al (2002) A new method for lumbar herniated inter-vertebral disc diagnosis based on image analysis of transverse sections. CMIG 26(6):369–380
18. Michopoulou SK, Costaridou L, Panagiotopoulos E, Speller R, Panayiotakis G, Todd-Pokropek A (2009) Atlas-based segmentation of degenerated lumbar intervertebral discs from mr images of the spine. IEEE Trans Biomed Imaging 56(9):2225–2231
19. Alomari Raja' S, Corso Jason J, Chaudhary V (2010) Labeling of lumbar discs using both pixel- and object-level features with a two-level probabilistic model. IEEE Trans Med Imaging (in press)
20. Liu F, Zhao B, Kijewski PK, Wang L, Schwartz LH (2005) Liver segmentation for ct images using gvf snake. Med Phys 32(12): 3699–3706
21. Videman T, Batti MC et al (2006) Determinants of the progression in lumbar degeneration: a 5-year follow-up study of adult male monozygotic twins. Spine 31:671–678
22. Niemeläinen R, Videman T et al (2008) Quantitative measurement of intervertebral disc signal using mri. Clin. Rad 63(3):252–255
23. Mulconrey D, Knight R (2006) Interobserver reliability in the interpretation of diagnostic lumbar mri and nuclear imaging. Spine 6:177–184